Paper No. 1019. (quote when citing this article)
Eleventh World Conference on Earthquake Engineering
ISBN: 0 08 042822 3

EFFECT OF EXCITEMENT FREQUENCY ON THE DYNAMIC STABILITY OF DILATIVE GRANULAR SLOPE

Kazuo KONAGAI and Takashi MATSUSHIMA

Institute of Industrial Science, University of Tokyo
Roppongi, Minato-ku, Tokyo 106, Japan

ABSTRACT

In studying the earthquake resistance of such dilative granular slopes as rockfill dams, rock mounds and etc., the slope stability is usually estimated assuming Coulomb's friction on internal shear planes. Some experimental studies, however, suggested that the acceleration required to initiate the slope failure of this kind tends to increase as the excitement frequency increases. Irreversible deformation of a granular slope is mainly due to a change in its fabric, and this process is accompanied by a noticeable dilation. This feature has been visually confirmed by means of the Laser-Aided Tomography (LAT), which allows the 3D image of deformation of granular assemblage models to be visualized. Based on the findings obtained in the coarse of LAT experiments, a simple conceptual model of surface slide, in which dilation yields the frequency dependence of the failure acceleration, is presented.

KEYWORDS

Dilation; slope stability; frequency dependence; failure acceleration; Laser-Aided Tomography.

INTRODUCTION

In many earthquakes, rapid slides not only in natural but also in artificial granular slopes have been responsible for as much damage as all the other seismic hazards combined. Regarding the problem, pseudo-static methods, like the seismic coefficient method, has been widely used to estimate the slope stability. Though the methods of this kind have been offering a great deal of important insights into the potential risk, the estimations have not always been true to the actual features of damage. In 1984 West-Nagano earthquake ($M_s = 6.8$, focal depth = 2 km) for example, Makio dam, with the source-site distance of only 5 km, suffered minor damage like longitudinal cracks and the slight settlement of the embankment, even though the peak acceleration of 0.4 g is estimated to have been reached. The minor damage must be the proof that the slope of Makio dam have experienced the critical state. However, the serviceability of the dam after the earthquake, which depends mostly on the extent of deformation, was affected little. It is, therefore, noted that the pseudo-static methods provide the index of stability but no information on deformation associated with slope failure.

Assumptions for the physical characteristics of various subsurface materials may be another causes of over or under-estimating the slope stability. Coulomb's hypothesis is generally assumed on the internal surface of

sliding of interest. However, It has been pointed out by some researchers (Tamura *et al.*, 1972, Toyota *et al.*, 1985) that the acceleration required for a granular slope to slide varies with both excitement frequency and the representative size of grains making up the slope. This phenomenon is seemingly different from the one governed by Coulomb's hypothesis. This paper introduces an idea of the model in which the dilating process of a granular shear band is responsible for the frequency dependence of failure acceleration.

VISUALIZATION OF FAILURE PROCESS

Konagai *et al.* (1994) visualized, by means of a new visualization method, Laser-Aided Tomography (LAT: Konagai *et al.*, 1992), that a sudden surface slide is attended by a noticeable dilation. According to LAT, particles of crushed glass are piled up in a water tank full of liquid which has the same refractive index as the glass. Consequently, the model becomes transparent and invisible in the liquid. An intense laser-light sheet (LLS), which is then passed through the model, illuminates the contours of all particles within the optically cut cross-section (Fig. 1).

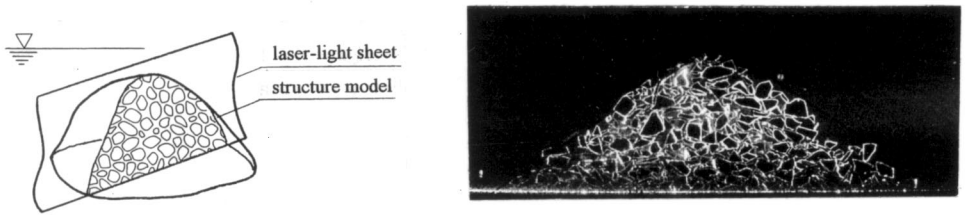

Fig. 1 Laser-Aided Tomography

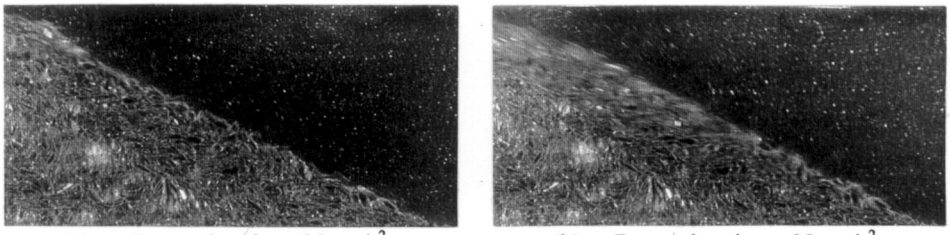

(a) t = 5s, acceleration =20 cm/s^2 (b) t =7s, acceleration = 28 cm/s^2

Fig. 2 Cross-section of embankment-shaped model

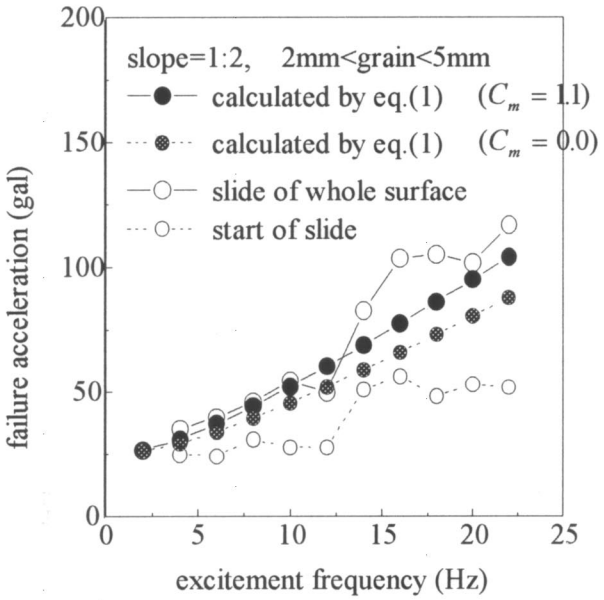

Fig. 3 Variation of failure acceleration with frequency

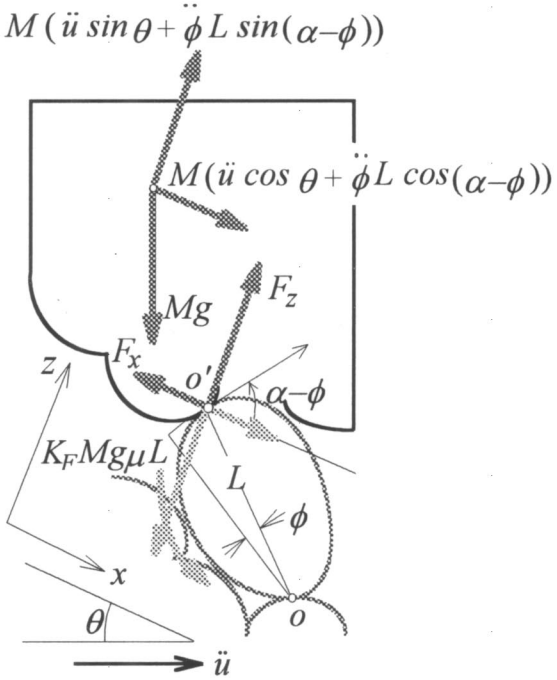

Fig. 4 Original model of surface slide

Dynamic failure tests of embankment-shaped models on a shaking table were conducted utilizing LAT. Screened glass grains serving as a model were piled up into an isosceles shape (height = 90 mm, slope = 1:2). An increasing sinusoidal shake was given to the model's base. The embankment's surface began to slide with a noticeable dilation no sooner than the base acceleration went up above a threshold (Fig. 2). Fig. 3 shows the variation of the threshold acceleration with the excitement frequency. The threshold increases with increasing excitement frequency, and the bigger the representative grain size is, the clearer the tendency is.

Taking into account the dilation observed in the LAT experiments, The authors (Konagai *et al.*, 1994) have presented a conceptual model for the surface slide of a coarse particle assemblage (Fig. 4). In their original model, the sliding surface mass is assumed to consist of a number of lumps of grains. One of the lumps, M, slides down the slope after once being pushed up on the rugged sliding surface. During this process, the lump M slips in the orbit of radius L (representative grain size) through an angle ϕ. According to their model , the half-sine-wave acceleration pulse ($= a \sin \omega t$, $0 < t < \pi / \omega$) required for the initiation of slide is obtained as:

$$a = g'(\theta_0 - \theta)\sqrt{1 + \frac{L}{g'}\omega^2} \tag{1}$$

where, θ is the inclination of the slope, which is assumed to be identical to the inclination of the internal sliding surface, θ_0 is the static angle of repose, and g' is given as:

$$g' = \frac{\gamma_g - \gamma_w}{\gamma_g + C_m \gamma_w} \tag{2}$$

in which, γ_g and γ_w are specific gravities of grain and liquid, respectively, and C_m is the added mass coefficient. The effect of dynamic change in pore pressure, which is to be discussed in the following chapter, has not been taken into account in the original model. Solid circles in Fig. 4 are given by eq. (1). All the curves connecting both the solid and open circles in Fig. 4 are upward to the right, showing the dependence on frequency of the threshold acceleration. However, when the subsurface material is made up of a variety of grains with different shapes and sizes for example, it will be extremely difficult to determine the representative grain size in eq. (1). Even though the simple conceptual model of this kind has a number of good features, the parameters for the model must be carefully determined. The following section is, thus, addressed to the revision of the model from the geotechnical point of view.

REVISED CONCEPTUAL MODEL

A soil column is cut out of an immersed embankment as shown in Fig. 5. In this figure, dM $(=\rho dz)$ is the mass of soil element with thickness dz. θ is inclination of shear band, u and u_{bottom} are plastic displacement of soil column and the displacement given to the base of the column, γ $(= \partial u / \partial z)$ is plastic shear strain, and F_x and F_z are effective reaction force components in x and z directions, respectively. Pore pressure p is resolved into dynamic and static terms as:

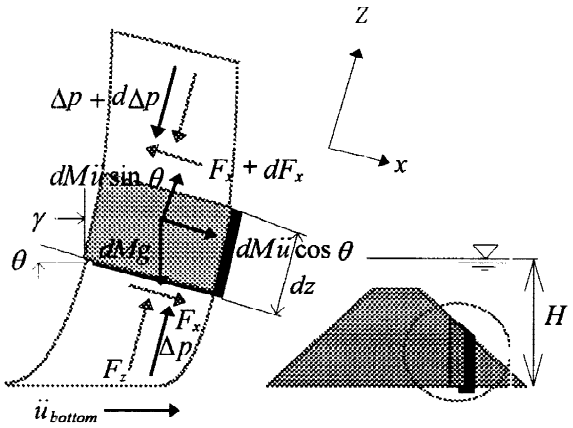

Fig. 5 Soil column cut out of a submerged embankment

$$p = \Delta p + \rho_w g(H - z\cos\theta) \tag{3}$$

where, Δp = dynamic change in pore pressure and $\rho_w g(H - z\cos\theta)$ = static water pressure. The equations of motion governing the plastic deformation of the submerged soil column are given as:

$$\rho \cdot dz \cdot (\ddot{u}\cos\nu + \ddot{u}_{bottom}\cos\theta) = \rho' \cdot dz \cdot g\sin\theta - \frac{\partial F_x}{\partial z}dz$$
$$\rho \cdot dz \cdot (\ddot{u}\sin\nu + \ddot{u}_{bottom}\sin\theta) = -\rho' \cdot dz \cdot g\cos\theta - \frac{\partial F_z}{\partial z}dz - \frac{\partial \Delta p}{\partial z}dz \tag{4-1), (4-2}$$

where, $\rho' = \rho - \rho_w$ in which ρ and ρ_w are the densities of water-saturated soil column and water, respectively, and ν is the angle of dilation. F_x and F_z satisfy the following equation as:

$$F_x = -F_z \tan\phi_{mob} \tag{4-3}$$

In the above eqs. (4.1)-(4.3), $\sin\nu$, $\sin\theta$ and $\tan\phi_{mob}$ are approximated by their angles ν, θ and ϕ_{mob}, respectively, and cosines of these angles approximate 1. It is also assumed that the acceleration normal to the shear band is negligibly small. These assumptions simplifies the above equations (4.-1)-(4-3) as:

$$\rho\ddot{u} = \rho' g\theta - \frac{\partial F_x}{\partial z} - \rho\ddot{u}_{bottom}$$
$$\rho' g = -\frac{\partial F_z}{\partial z} - \frac{\partial \Delta p}{\partial z} \tag{5-1)-(5-3}$$
$$F_x = -F_z\phi_{mob}$$

It is assumed that the granular column is completely saturated with incompressible water. Therefore, the dilating process of the subsurface material would yield negative pore pressure that would enhance the slope stability. Though the flow induced by shearing the material may be laminar or turbulent flow depending on many factors such as the extent of dilation, strain rate and permeability, Darcy's law is used, in the first place, to incorporate the pore pressure effect. Darcy's law is written for the granular column as:

$$\dot{w} = -\frac{k}{\rho_w g}\frac{\partial(p + \rho_w gz)}{\partial z} = -\frac{k}{\rho_w g}\frac{\partial \Delta p}{\partial z} \tag{5-4}$$

Assuming the incompressibility of water, the change in the flow velocity with respect to z, $\partial\dot{w}/\partial z$ is expressed in terms of the void ratio e as:

$$\frac{\partial \dot{w}}{\partial z} = -\frac{\partial e}{\partial t} \tag{6}$$

During the process of plastic deformation, increasing rate of the void ratio $\partial e/\partial t$ is written as:

$$-\frac{\partial e}{\partial t} = -\nu\frac{\partial \gamma}{\partial t} \tag{7}$$

Differentiating eq. (5-4) with respect to z, and equating it with eqs. (6) and (7), the following equation is obtained:

$$\nu\frac{\partial \gamma}{\partial t} = \frac{k}{\rho_w g}\frac{\partial^2 \Delta p}{\partial z^2} \tag{8}$$

Eq. (5-2) is integrated with respect to z as:

$$F_z = \rho' g(H - z) - \Delta p = M' g - \Delta p \tag{9}$$

Differentiating eq. (5.3) with respect to z, and using eqs. (5.2) and (9), the following equation is obtained:

$$\frac{\partial F_x}{\partial z} = -\phi_{mob}\frac{\partial F_z}{\partial z} - F_z\frac{\partial \phi_{mob}}{\partial z} = \phi_{mob}\left(\rho' g + \frac{\partial \Delta p}{\partial z}\right) - (M' g - \Delta p)\frac{\partial \phi_{mob}}{\partial z} \tag{10}$$

Substituting eq. (10) into eq. (5.1) results in:

$$\rho\ddot{u} = \rho' g\theta - \phi_{mob}\left(\rho' g + \frac{\partial \Delta p}{\partial z}\right) + \frac{\partial \phi_{mob}}{\partial z}(M' g - \Delta p) - \rho\ddot{u}_{bottom} \tag{11}$$

During the shearing process of the element, the stress-dilatancy equation is well approximated by the following equation ("saw-blades model", Fig. 6, Bolton, 1986):

$$\phi_{mob} = sign\left(\frac{\partial^2 u}{\partial z \partial t}\right)\cdot\mu + \eta\cdot\nu \tag{12}$$

where, μ is the critical angle of shearing and ν is the angle of dilation. η should be 1 as far as the saw-blades

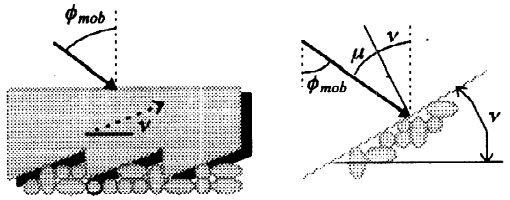

Fig. 6 Saw-blades model of dilatancy

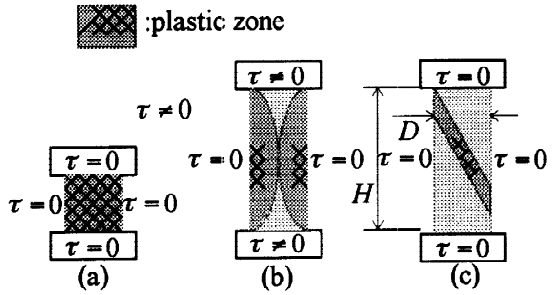

(a) smooth interface H/D=1
(b) rough interface H/D=2.7
(c) smooth interface H/D=2.7

Fig. 7 Outline of triaxial test run

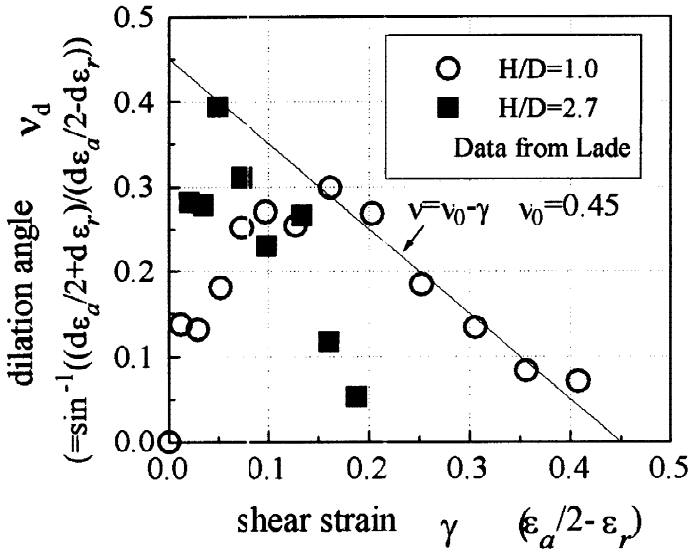

Fig. 8 Variation of dilation angle with shear strain

model (Fig. 6) is adopted. However, Bolton showed that setting η at 0.8 yields the better agreement, being based on the published triaxial and plane strain data for 17 different sands. The angle of dilation varies with respect to the increasing shear strain ($=\partial u/\partial z$). Various relationships regarding the dilating process are available in many papers. It is, however, not easy to obtain a reliable variation of dilation angle with shear strain especially beyond the peak strength of soil because strain localization develops within a specimen.

A number of triaxial tests have been performed in Denmark on the short and thick specimens (height-diameter ratio H/D = 1) with smooth interfaces on both ends (Fig. 7: Lade 1982, Ibsen 1994). Using the thick specimens have surely contributed to avoid strain localization to a great extent, and provided a great deal of insights into the dilating process of granular material. A triaxial test itself does not provide the clear physical illustration of the dilating process that is provided by a plane strain test. Matsuoka , however, explained that the strain state within a triaxial specimen can be resolved into two independent shear components orthogonal to each other. Given the axial and radial strain increments, $d\varepsilon_a$ and $d\varepsilon_r$ within a triaxial specimen, the components of principal strain increment accompanied by the two-dimensional shearing are denoted by $d\varepsilon_a/2$ and $d\varepsilon_r$, with which the dilation angle is obtained. Fig. 8 shows one example of the variations of the dilation angle with respect to the shear strain γ ($=\varepsilon_a/2-\varepsilon_r$), which is based on the published data (Lade 1982). Solid squares are obtained in the conventional way, whereas open circles are from the triaxial test performed on the short and thick specimens. Since the void ratio and the strains at both the peak strength and ultimate states are underestimated in the conventional triaxial test ($H/D=2.7$), the dilation angle drops faster than the one by the Danish triaxial test. Relying on the triaxial test with the thick specimens, the relation between the dilation angle and the shear strain above the peak strength would be roughly expressed in the following form as:

$$\nu=\begin{cases} sign(\gamma)\cdot\nu_0-\gamma & 0<|\gamma|<\nu_0 \\ 0 & \nu_0<|\gamma| \end{cases} \tag{13}$$

Substituting eqs. (12) and (13) for $0<|\gamma|<\nu_0$ into eq. (11), and noting that $\gamma=\partial u/\partial z$ for the soil column in Fig. 7, the following equation of motion is finally obtained:

$$\begin{cases} (\nu_0-\dfrac{\partial u}{\partial z})\dfrac{\partial^2 u}{\partial t\partial z}=\dfrac{k}{\rho_w g}\dfrac{\partial^2\Delta p}{\partial z^2} \\ \rho\ddot{u}=\rho' g\theta-\left(\rho' g+\dfrac{\partial\Delta p}{\partial z}\right)\left(sign\left(\dfrac{\partial^2 u}{\partial z\partial t}\right)\cdot\mu+sign\left(\dfrac{\partial u}{\partial z}\right)\cdot\eta\cdot\nu_0-\eta\dfrac{\partial u}{\partial z}\right)-\dfrac{\partial^2 u}{\partial z^2}(M' g-\Delta p)-\rho\ddot{u}_{bottom} \end{cases}$$

(14-1), (14-2)

It is noted that eq. (14-2) is valid only when the shearing is being developed. When the element is in the sticking state, the following equation should be satisfied because the element behaves like a rigid body:

$$\frac{\partial^2 u}{\partial z \partial t} = 0 \tag{15}$$

NUMERICAL EXAMPLES

To conduct the time domain analysis by means of the present conceptual model, the finite difference method is adopted. Taking the LAT-model size for example, a small-size (10 cm) granular column is considered. A simple half sine pulse ($= a \sin \omega t \quad (0 < \omega t < \pi), a = 2.0\ \mathrm{m/s^2}, \omega / 2\pi = 2.0\ \mathrm{Hz},$) is given to the base of the column so that the column deforms monotonically in x direction. The mechanical properties of the material are shown in Table 1.

Table 1 Mechanical properties of the granular material

mass density ρ (t s^2/m^4)	critical angle of shear μ	maximum dilation angle ν_0	inclination of shear band θ	permeability coefficient k (m/s)
0.16	0.32	0.4	0.5	10^{-3}

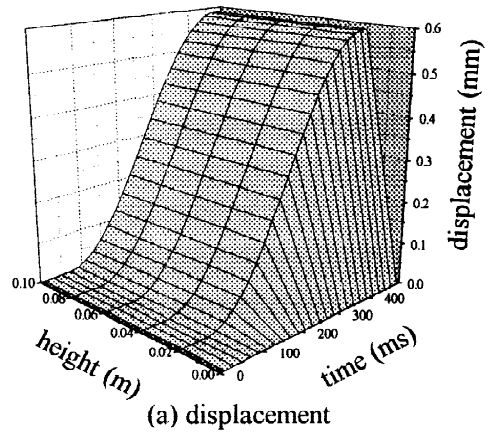

(a) displacement

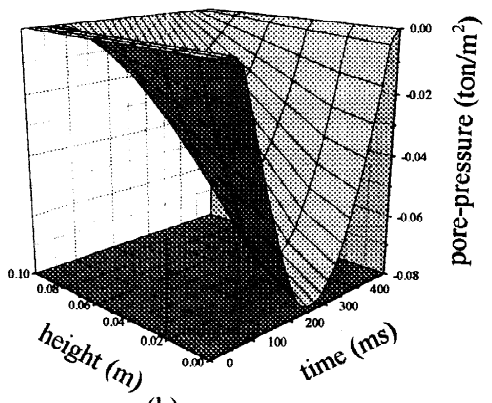

(b) pore pressure

Fig. 9 Time histories of displacement and pore pressure distribution within column (k=10^{-3} m/s)

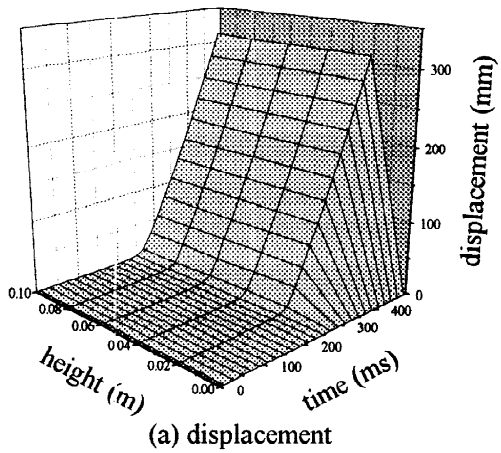

(a) displacement

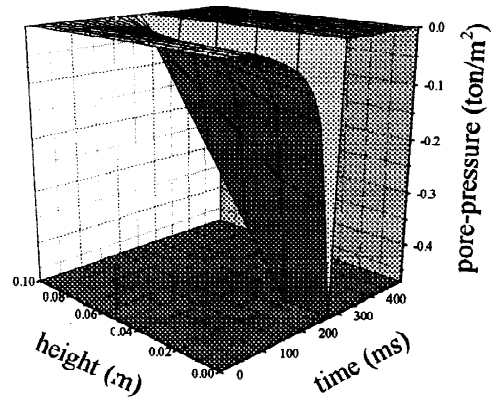

(b) pore pressure

Fig. 10 Time histories of displacement and pore pressure distribution within column (k=10^{-2} m/s)

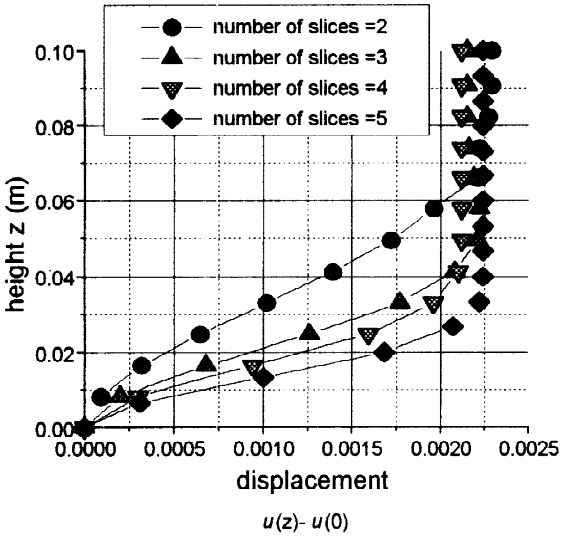

Fig. 11 Deformation modes

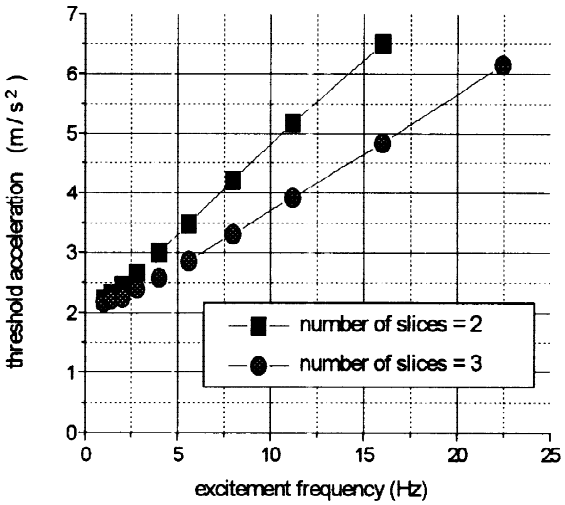

Fig. 12 Variation of threshold with frequency

Figs. 9 (a) and (b) show the displacement and pore pressure time histories of the column. Deformation of the column starts as soon as the base acceleration of 220 cm/s^2 ($=\mu+\nu_0-\theta$) is reached. After this value is reached, the bottom element begins to deform carrying its upper part. During this process, negative pore pressure is developed within the column (Fig. 9(b)). The pore pressure distribution has its bottom value at the bottom end of the column, and its minimum value is reached when the shear strain rate reaches its maximum. Beyond this point, the negative pore pressure lessens as the strain rate lessens. The elements stick to each other again at about 0.48 s, and keep sticking after that.

Figs. 10 (a) and (b) show the time histories of displacement and pore pressure within a granular column whose mechanical properties, except for the permeability coefficient, are kept unchanged. Since the permeability has been increased by 10 times, the deformation of the column develops much faster than the previous example. The rapid increase in shear deformation is accompanied by the sudden drop in pore pressure within the column. The negative pore pressure, however, disappears suddenly as soon as the bottom element reaches its ultimate state of shearing, because no dilation occurs beyond this point. These two examples show the noticeable effect of pore pressure on the development of submerged surface slide. The negative pore pressure provides a submerged surface with the suction which enhances the slide resistance of the slope.

The finite difference method, however, does not provide the detailed illustration of the deformation within a sliced element. For the closer examination of the shear-banding process, the effect of pore pressure is temporary excluded in the following discussion. Exclusion of the pore-pressure effect in eq. (14-2) yields:

$$\ddot{u} = g\left(\theta - sign\left(\frac{\partial^2 u}{\partial z \partial t}\right)\cdot\mu - sign\left(\frac{\partial u}{\partial z}\right)\cdot\eta\cdot\nu_0 + \eta\cdot\frac{\partial u}{\partial z}\right) - \frac{M' g\eta}{\rho'}\frac{\partial^2 u}{\partial z^2} \tag{16}$$

The displacement within a slice is then assumed to be expressed in a cubic polynomial form. Four unknown constants of this polynomial are so determined as to satisfy the four boundary conditions at both ends of the element. Either eq. (16) in the slipping state or eq. (15) in the sticking state should be satisfies at both ends of the element. The transfer matrix is formulated using these two equations. Fig. 11 shows the deformation modes of the column 0.067s after being subjected to a half sine pulse, and Fig. 12 shows the variation of threshold with the excitement frequency. This variation is clearly affected by the element' size, namely, on the thickness of shear band. The variation is much more pronounced as the shear band becomes thicker. According to eq. (1) showing the threshold acceleration for the original model, the best fit to the curve in Fig. 11 is obtained by setting L at 0.0077 for N=2, and at 0.0044 for N=3. This equivalent L seems to be about 1/10-1/7 of the shear band width shown in Fig. 11 , or may be comparable with the representative grain size

which is usually about 1/20-1/10 of the thickness of shear band. If the shear strain distribution within a shear band were homogeneous, the L could be rationally replaced with the thickness of shear band. The distribution of shear strain, however, is not homogeneous and has the shape with its maximum value reached just in the midst of the band.

CONCLUSIONS

A simple conceptual model of surface slide, in which dilation leads to the frequency dependence of failure acceleration, was presented. The behavior of a simple shear soil column cut out of an immersed granular embankment was discussed. The column virtually includes continuously distributed shear planes, thus, allowing the column to deform continuously. The conclusions obtained through the study are summarized as follows:

(1) The shearing process of dense and water-saturated subsurface material induces noticeable suction which enhances the slide resistance of the slope even though the permeability coefficient is large enough to be comparable with that of gravely material.

(2) Both the cubic shape function and the element's size govern the thickness of shear band in the present model. Thus, the size of element must be determined taking into account the actual shear band's behavior. The thicker the shear band is, the clearer the frequency dependence of failure acceleration is.

(3) The maximum shear strain is reached in the about middle of shear band thickness. The maximum shear strain is much bigger than the overall shear strain within the shear band, thus, affects much the slope stability.

REFERENCES

Bolton, M. D. (1986): The strength and dilatancy of sands, *Geotechnique*, **36**, **1**, 65-78.

Ibsen, L. B. (1994). The stable state in cyclic triaxial testing on sand, *Soil Dynamics and Earthquake Engineering*, **13**, 63-72.

Konagai, K., C. Tamura, P. Rangelow and T. Matsushima (1992). Laser-Aided Tomography: A tool for visualization of changes in the fabric of granular assemblage, *Structural Engineering / Earthquake Engineering*, Japan Society of Civil Engineers, **9**, **3**, 193s-201s.

Konagai, K., T. Matsushima and T. Sato (1994). Dependence on frequency of dynamic inter-particle dislocation within a slope, *Structural Engineering / Earthquake Engineering*, Japan Society of Civil Engineers, **11**, **2**, 93s-101s.

Lade, P. V. (1982). Localization effects in triaxial test on sand, *IUTAM Conference on Deformation and Failure of Granular Materials*, A. A. Balkema, Rotterdam.

Matsuoka, H. (1974). Dilatancy characteristics of soil, *Soils and Foundations*, **14**, **3**, 13-23.

Tamura, C., S. Okamoto and K. kato (1972). Failure tests on rockfill dam models, *Jour., Japan Society of Soil Mechanics and Foundation Engineering*, **20**, 7.

Toyota, M., M. Shiga and N. Matsumoto (1985). Experimental study of the effect of grain size on seismic slope stability, *Proc., 18th Earthquake Engineering Congress*, Japan Society of Civil Engineers, 449-452.